

Identifying ENSO-Related Interannual and Decadal Variability on Terrestrial Water Storage

Se-Hyeon Cheon (✉ shcheon95@gmail.com)

Jet Propulsion Lab

Benjamin Hamlington

Jet Propulsion Lab

John Reager

Jet Propulsion Lab

Hrishikesh Chandanpurkar

Jet Propulsion Lab

Research Article

Keywords: TWS, ENSO, interannual, water

Posted Date: February 17th, 2021

DOI: <https://doi.org/10.21203/rs.3.rs-199961/v1>

License: © ⓘ This work is licensed under a Creative Commons Attribution 4.0 International License.

[Read Full License](#)

Identifying ENSO-related interannual and decadal variability on terrestrial water storage

S.-H. Cheon^{1,*}, B. D. Hamlington¹, J.T. Reager¹, and H. A. Chandanpurkar¹

¹Jet Propulsion Laboratory, California Institute of Technology, Pasadena, CA 91109, USA.

*shcheon95@gmail.com

Abstract

We apply two statistical techniques to satellite measurements to identify a relationship between terrestrial water storage (TWS) and El Niño-Southern Oscillation (ENSO). First, we modified and used the least-squares regression of a previous study using longer records. Second, we applied a cyclostationary empirical orthogonal function analysis (CSEOF). Although the CSEOF technique is distinct from the LSR in that it does not consider proxies, each method produces two modes (decadal and interannual), showing consistency with each technique in spatial pattern and its evolution amplitudes. We also compared the results obtained by the two methods for 30 watersheds, of which five watersheds were compared with previous studies. The combination of the two modes explains the total variance in most river-basins showing the role that interannual and decadal ENSO-related signals in understanding terrestrial water storage variability. The results show that the decadal mode, along with the interannual mode, also plays an important role in describing the local TWS.

Introduction

Terrestrial water storage (TWS) represents vertically integrated water storage systems over land and includes water stored in tree canopies, surface water, soil, groundwater, snow, and ice¹. While little is known about the absolute amount of TWS, it directly relates to water availability for human and ecosystem use and is of interest to a range of local to regional scale water resources researchers and managers. Changes in TWS also correspond to water mass movement between land and ocean and have recently emerged as the dominant cause of interannual variability in global mean sea level²⁻⁴. Many studies indicated that regional imbalances and extreme changes in TWS caused by human activities have been increasing, and this trend is expected to continue in the current century⁵⁻⁷. Under these circumstances, it is essential to properly understand the change of TWS and predict the change of TWS based on the understanding in terms of securing stable water resources for human beings and the ecosystem. In particular, the understanding of the natural variability of TWS can provide essential information for estimating human-induced TWS change and also can be used to predict the near future variability of TWS by combining it with predictive information from connected climate modes. Many studies have been carried out to quantify natural fluctuations in TWS and separate these from possible anthropogenic influences⁸⁻¹². One of the primary drivers of the natural variability of TWS is the El Niño-Southern Oscillation (ENSO), and its global and regional influence has been described in many studies¹³⁻¹⁸.

Among studies investigating the ENSO-related TWS signal, few have been conducted on a global scale, and most have relied on comparisons to climate indices tracking the strength of ENSO. Ni, et al.¹⁸, for example, found that interannual TWS changes are strongly correlated with ENSO over much of the globe using multiple data sources, focusing on five river-basins. When it comes to global scale studies, Phillips et al.⁹ (hereafter PH12) estimated the global TWS signal using satellite-measured TWS data over 2003-2010 associated with ENSO by applying a least-squares regression (LSR) leveraging the Multivariate

ENSO Index (MEI) ¹⁹. While PH12 suggests a relationship between ENSO and TWS variability in the globe, questions remain regarding the degree to which the MEI represents ENSO and the appropriateness of the underlying technique itself (see Chao and Chung ²⁰; hereafter CC19). PH12 was conducted on only eight years of data, and with the influence of longer-timescale natural variability during this period, the degree to which ENSO influences can be separated from other variability is challenging to assess ²¹.

A non-parametric approach such as Empirical Orthogonal Function (EOF) or Cyclostationary EOF analysis (CSEOF) ^{22,23} has a potential benefit as it does not depend on the predefined climate indices such as MEI and Pacific Decadal Oscillation (PDO) ^{24,25}. EOF and CSEOF analysis decompose spatio-temporal data into the statistical modes in the order of each mode's variance. Various studies have applied CSEOF analysis to decompose climate datasets into independent modes representing natural variabilities ^{3,21,22,26-28}. The most challenging CSEOF analysis issue is interpreting the decomposed statistical mode, and the previous studies have tried to link the decomposed mode to predefined climate indices.

This study aims to identify and isolate the ENSO-related variability in TWS using the two techniques for satellite measurement. In the first approach, we update and modify the technique of PH12 using the longer data record now available and improved the treatment and use of MEI to respond to the CC19's concerns. The second approach relies on CSEOF analysis by identifying the ENSO-related statistical modes. After extracting the ENSO-relating TWS variabilities from both techniques, we examine the isolated TWS changes on both global and regional scales.

Data and Methods

Terrestrial Water Storage Data

While TWS has traditionally been a problematic state variable to measure globally²⁹, monthly global observations of TWS change have been made possible by the Gravity Recovery and Climate Experiment (GRACE) mission since 2002^{30,31}. GRACE data have been widely used in hydrology research from regional to global scale on topics such as hydrologic extremes, human water management, changes in surface water, lakes and reservoirs, and groundwater, and the natural and forced variability in storage at multiple time scales (see McCabe, et al. ³² for a summary). The first GRACE satellites ceased their mission in 2017 after roughly fifteen years of operations, and GRACE Follow-On (GRACE-FO) has been measuring changes in TWS since May 2018 ³³.

In this study, we used RL06M Version 2.0 GRACE MASCON Solution dataset generated by NASA Jet Propulsion Laboratory; in this dataset, a 3x3 mascon has one representative value to minimize the observation error^{31,33-35}. This gridded dataset has a one-month temporal and 0.5-degree spatial resolutions, and we extracted land from Jan 2003 to Dec 2016 due to the missing period between GRACE and GRACE-FO.

Least-Squares Regression

PH12 extracted TWS variability at each grid point of the GRACE data using the MEI and Hilbert-transformed MEI as independent variables in an LSR (Equation 1). PH12 then estimated the amplitudes and phases using regression coefficients to assess the relationship between ENSO and TWS variability at each location around the globe; the amplitudes represent the ENSO's influence on TWS, and the phase shows the lag between MEI and corresponding TWS changes.

$$T(r, t) = Const(r) + m_1(r) \times MEI(t) + m_2(r) \times MEI_H(t) \quad (1)$$

where $T(r, t)$ is a space-time (r and t) data, $Const(r)$ is the constant parameter, $m_1(r)$ and $m_2(r)$ are LSR parameters for independent variables, $MEI_H(t)$ is the Hilbert-transformed $MEI(t)$.

PH12 was conducted on only eight years of data, which is insufficient to capture the influence of longer-timescale natural variability²¹. Also, post-2010, there were two major ENSO events: the 2010-2011 La Niña, which caused the global mean sea level to drop by 7 mm and the 2015-2016 El Niño, one of the biggest in satellite observation era¹³. The inclusion of these extreme events in the current analysis is likely to increase the identified ENSO-TWS relationship's robustness.

As a potential remedy to problems arising CC19, we increase the number of independent variables in the regression and separate timescales of variability by decomposing the MEI into decadal variability (or Decadal Climate Index, hereafter DCI) and interannual variability (or Interannual Climate Index, hereafter ICI) following Zhang and Church³⁶. We estimated DCI by applying a low-pass filter to the MEI in successive 25 and 37 months moving averages. This is different from Zhang and Church³⁶ which used a PDO index to compute the DCI. Here, we are interested in ENSO-related variability and ensuring independent indices, so we used the MEI to compute both the ICI and DCI. After subtracting the DCI from MEI, the remaining signal is the ICI (Figure 1a). Four independent variables were created by Hilbert transforming both DCI and ICI, and the parameters of each independent variable were calculated through Equation (2):

$$T(r, t) = Const(r) + d_1(r) \times DCI(t) + d_2(r) \times DCI_H(t) + i_1(r) \times ICI(t) + i_2(r) \times ICI_H(t) \quad (2)$$

where $d_1(r)$, $d_2(r)$, $i_1(r)$, and $i_2(r)$ are LSR parameters, and $DCI_H(t)$ and $ICI_H(t)$ are the Hilbert-transform of $DCI(t)$ and $ICI(t)$. Following PH12, we analyzed the ENSO-related changes quantitatively by applying Equation (3):

$$AMP = \sqrt{A_r^2 + A_i^2} \quad (3)$$

where A_r and A_i are LSR parameters of the Hilbert-transformed index A .

We removed annual signals and linear trends at each grid location like PH12 before applying the LSR. Then, we estimated the TWS amplitudes of MEI, DCI, and ICI but did not apply the phase analysis of PH12 because of its inaccuracy (CC19).

Cyclostationary EOF Analysis

CSEOF analysis decomposes spatiotemporal data into spatial patterns (or Loading Vector, hereafter LV) and its temporal evolutions (or Principal Component Time-series, hereafter PCT) for each mode. It is similar in structure to the widely used EOF analysis (Equation 4), although with the notable difference that the spatial patterns of each mode are periodic, with a specific nested period (Equation 5).

$$T(r, t) = \sum_i LV_i(r, t) \times PCT_i(t) \quad (4)$$

$$LV(r, t) = LV(r, t + d) \quad (5)$$

where $T(r, t)$ is the space-time data being decomposed, $LV(r, t)$ is the loading vector, $PCT(t)$ is the principal component time-series, and d is a nested period.

The nested period's determination plays a critical role in the CSEOF analysis, especially when targeting specific frequencies, as in this study. Based on previous studies^{21,37,38} about ENSO variability, we chose a 24-month nested period. This two-year nested period allows for the separation of ENSO's biennial oscillation (i.e., the transition between warm and cold events) and lower-frequency variability found centered in the Pacific Ocean. The references above give further justification for the use of this nested period. Before applying CSEOF analysis, we preprocessed the dataset like the LSR analysis.

Results and discussion

Least-Squares Regression

We used and modified PH12 to estimate ENSO-related TWS from the GRACE data over 2003-2016. Figure 1b-d show the amplitude maps resulting from these analyses. The amplitude map relating to MEI (Figure 1b) has relatively large signals in southern Africa, South America, the Antarctic coast, and Greenland. This pattern is generally similar to PH12, but it shows differences in Eastern Asia, South America, Greenland, and northern Australia. This difference may be in part to using six additional years of data compared to PH12, as stated in CC19.

This study further decomposed the MEI into DCI and ICI and applied it to the newly proposed LSR (Equation 2). Figure 1c and d show the amplitudes associated with the DCI and ICI, respectively. The ICI's amplitude map has relatively large values in southern Greenland, South America, and the southeastern United States. The DCI has large amplitudes in other regions, such as southern Africa, South America, North America, and Greenland. Comparing to the MEI map, the DCI and ICI maps appear to be decomposing the result using only the MEI into interannual and decadal components. The similarity between the two maps is not unexpected, given the MEI decomposition in the approach's structure. For example, significant values in the amplitude using the MEI (see southern Africa, the eastern part of Australia, the southern part of South America, and Central Asia) do not appear in the ICI pattern. These disagreements suggest that larger amplitude areas are mainly represented by the DCI, which is difficult to ascertain using the original LSR from PH12

While these results do not conclusively tie TWS variability at every location with large amplitudes to ENSO, they demonstrate the climate index-based approach's potential problems. The range of timescales represented by the MEI can lead to the suggestion that the phase transition from El Niño to La Niña, for example, plays a significant role in the variability at a given location, when there is substantial lower-frequency variability that is driving TWS change at that location.

CSEOF analysis and comparison with LSR

Ten CSEOF's modes explained 99.9% of GRACE data's total variance, and the first two dominant modes explained 31% and 21% of the total variance, respectively. Figure 2 shows the two dominant CSEOF modes, and the two modes are highly correlated with ENSO. The correlation coefficient (ρ) between a smoothed MEI (6-month moving averaged) and the first and second modes' spatial-mean time-series (obtained by combining the PCT and spatial-mean of the LV) are -0.55 and -0.39, respectively. The ρ -values are significant at the 99.9% confidence level, and in other modes, ρ - values' magnitudes were less than 0.10. Also, the areas having relatively

strong signals in the first and second modes are generally in line with areas known as ENSO-correlated regions^{9,13,18,39}.

In the first mode (Figure 2a and c), the spatial patterns change little throughout the 24-month nested period, indicating that the dominant physical process described has a temporal evolution of substantially longer than the chosen nested period; the PCT varies only over relatively long timescales. Therefore, coupling the LV and PCT, we refer to this mode as the low-frequency (LF) mode and representative of variability on decadal timescales. In the second mode (Figure 2b and d), the LV shows more significant changes than the first mode. In many locations, the LV shows a complete cycle of phase transition throughout the 24-month nested period (see the Amazon basin, for example), and the period of PCT is shorter than the first mode. Therefore, we will call this mode the high-frequency (HF) mode representing interannual variability.

To further investigate these modes, we compare the CSEOF modes to the LSR modes. As constructed, the LSR approach extracts TWS signals corresponding to MEI's lower and higher-frequency components (DCI and ICI). The LSR subsequently produces two corresponding spatial patterns: one for ICI-mode and DCI-mode. First, we compare DCI-mode and LF-mode. The ρ -value between the PCT of the LF-mode and DCI is high as 0.90, and the spatial patterns of the two modes are also very consistent in most areas (Figure 1c and Figure 2a). From these results, we conclude that the DCI-mode and LF-mode are very similar, and they represent the same variabilities on TWS.

To compare the ICI-mode and HF-mode, we recover the HF-mode spatiotemporal signals by combining the HF-mode's LV and PCT. Then, we compute the global spatial-mean time-series of the HF-mode and compare it to the ICI, obtaining ρ of -0.40 (Figure S1). The negative correlation is in line with the fact that ENSO events' negative phase increases TWS globally and reverses during the positive phase (e.g., Boening, et al.¹³). Locations showing substantial variability are similar in both higher-frequency modes, e.g., Australia and Southern Africa. We can see the LF-mode and ICI mode are related to each other, although the similarity is weaker than the lower frequency modes.

Local ENSO-related TWS

The two approaches were compared in thirty river-basins to estimate dominant drivers of the regional TWS changes (basins' information obtained from Mandate and Compact⁴⁰; see Table 1. Among the thirty-basins, we examined five-basins (Amazon, Burdekin, Ganges-Brahmaputra, Mississippi, and Zambezi) in detail. Before the analysis, we made basins' spatiotemporal datasets: original GRACE data with no annual and linear trend signals, TWS by modified LSR, TWS combining LF and HF-modes, TWS of LF-mode, and TWS of HF-mode. The spatial-mean time-series were estimated in each river-basin using these datasets. The five-basins' resulting time-series and the percentages of variance explained in the total TWS are shown in Figure 3 and Table 1.

Previous studies have shown that TWS in the Amazon River is correlated with ENSO^{9,18}. Chen, et al.¹⁴ showed that ENSO is related to extreme TWS changes such as floods and drought in the Amazon river-basin. Figure 3a shows consistency with Chen, et al.¹⁴, showing that 2015-2016 El Niño (2010-2011 La Niña) causes drought (flood). However, basin-wide comparisons are complicated because the dynamic spatial variance presented in this region creates difficulties in explaining the regional TWS using an ENSO index. LSR and CSEOF show similar performance

by explaining 45.6% and 49.1% of total TWS in this area, and HF and LF-modes describe 28.7% and 20.4% of total TWS. The HF-mode is related to the ICI and explains only 28.7% of TWS. Therefore, the low-frequency driver plays an essential role in understanding the TWS of the Amazon River basin along with the interannual driver represented by ENSO.

Rainfall and river flow in the northeastern Queensland region of Australia are known to be linked to PDO and ENSO^{41,42}. The Burdekin River is also located in the northeastern Queensland region, and Lough⁴² showed that the river flow was correlated with Nino 3.4 and PDO (ρ -values of -0.29 and -0.28, respectively). In this study, the LSR and CSEOF describe 65.3% and 73.5% of the TWS of this area, respectively. The LF and HF-modes explain 62.9% and 10.6% of the total TWS, showing that the low-frequency driver is dominant. It is consistent with the Lough's results that rainfall and river flow in this area are closely related to PDO, although the connection between TWS and the low-frequency driver is more significant here than the Lough's results.

The Ganges-Brahmaputra River basin is negatively correlated with ENSO due to the decrease in TWS when El Niño occurs^{17,43,44}. In this region, CSEOF explains more of the TWS variance than the LSR, with LSR and CSEOF accounting for 22.6% and 51.9% of TWS, respectively. The HF and LF-modes account for 37.1% and 14.8% of TWS, indicating that ENSO is the primary driver of the TWS change. The regional average of the ρ -value of HF-mode is about -0.4 (Figure S1). Although ENSO is the primary driver, the LF-mode contributes significantly as well. For example, the TWS changes in Dec-2011 to Jan-2012 and Dec-2015 to Jan-2016 are challenging to explain without the LF-mode. Therefore, the interannual ENSO variability is the dominant driver of regional TWS changes, but the regional TWS can be explained better by also considering the low-frequency driver.

Many studies have been conducted to clarify the relationship between the water resources and ENSO in the Mississippi River basin⁴⁵⁻⁵⁰. Munoz and Dee⁴⁹ explained the increase in the probability of flooding after El Niño as the increase in rainfall in the southern Mississippi River basin due to El Niño and the resulting increase in soil moisture saturation. Thus, El Niño positively correlates with TWS in the southern part of the Mississippi River basin (Figure S1). However, it is challenging to explain the TWS of this basin using ENSO only because positive and negative relations exist simultaneously (Figure S1). In this area, LSR only accounts for 6.6% of TWS, whereas CSEOF can describe 51.5% of the region's TWS. Since ICI and DCI are used as proxies in LSR, this indicates that the proxies are not applicable to this area. HF and LF-modes account for 40.5% and 11% of the regional TWS, showing the HF-mode is dominant. The TWS of this region is linked to ENSO, but its impacts are not easy to separate from other TWS variability. It is challenging to describe the regional TWS using ENSO-related indices, but CSEOF's HF and LF-modes can better describe the regional TWS variability.

Gaughan, et al.²⁷ showed that El Niño (La Niña) was associated with an increase (decrease) in rainfall intensity in the Zambezi River basin. However, in this study, the HF and LF-modes account for 10% and 45.6% of the local TWS. The LF-mode explains far more variance than the HF-mode (Figure 3e, Table 1). The LSR and CSEOF account for 56.5% and 55.6% of the regional TWS, indicating that DCI and ICI are generally able to explain interannual to decadal variability in TWS in the region. Although we could not find strong evidence that TWS in this area is driven by ENSO variability, we did find the description of TWS is improved by including a separate representation of lower-frequency variability (either DCI or LF-mode).

Summary

To assess ENSO influence on TWS, we conducted LSR analysis after dividing MEI into a decadal index (DCI) and an interannual index (ICI) using the GRACE dataset over 2003-2016. Through the better separation of timescales, some of the issues raised in CC19 are addressed, and the resulting spatial patterns associated with ICI and DCI are obtained. This analysis shows that the amplitude map using only the MEI in PH12 is separable into two distinct timescales. While this separation may not be surprising, both timescales are represented in the MEI, highlighting the importance of decadal variability in TWS at many locations.

We also performed CSEOF analysis as a proxy-independent scheme, which separates spatiotemporal data into a modal description. It is difficult to assign a particular statistical mode-specific physical meaning, but the two dominant CSEOF-modes correspond with the LSR's results. The first CSEOF-mode connects closely to DCI-mode, with similar spatial variability and associated time-series. The second CSEOF-mode has an apparent two-year periodicity and a similar spatial pattern of ICI-mode.

To consider the regional impacts of the lower and higher-frequency modes, we evaluated the results of LSR and CSEOF in thirty watersheds, and five of them were selected for more detailed analysis. We confirmed the roles of the interannual and decadal variabilities of TWS in each region, and through this, we identified the ENSO impact on each region's TWS. Both interannual and decadal variabilities had essential roles in describing the regional TWS, and their roles differed in each area. Both methods showed consistent results with previous studies in most regions and accounted for the local TWS at similar levels in the Amazon, Burdekin River, and Zambezi River basins. However, in the Ganges-Brahmaputra River and the Mississippi River, the CSEOF analysis described the region's TWS far better than the LSR.

In conclusion, by modifying PH12's LSR and applying a new technique (CSEOFs), we have taken steps to isolate the ENSO-related TWS signals on a global scale. However, through the LSR analysis, potential problems have been identified with the approaches relying on a climate index that impose a particular structure on the extracted variability. In this respect, statistical decompositions such as CSEOF analysis are potentially advantageous in isolating and understanding the natural variability in TWS. This advantage will become more evident as more observations are accumulated in the future. Also, the estimation of ENSO's impact on thirty watersheds showed that the decadal and interannual changes' influences were different in each watershed. We expect the two methods shown in this study can contribute to increase the capability of water resource management by combining ENSO's short-term prediction scheme.

Data Availability

The JPL GRACE and GRACE-FO Mascon Ocean, Ice, and Hydrology Equivalent Water Height Coastal Resolution Improvement (CRI) Filtered Release 06 Version 1 can be obtained from NASA PO.DAAC, CA, USA, at <https://doi.org/10.5067/TEMSC-3JC62>.

All materials and correspondence requests can be directed to S.H. Cheon at shcheon95@gmail.com.

References

- 1 Oki, T. & Kanae, S. Global hydrological cycles and world water resources. *science* **313**, 1068-1072 (2006).
- 2 Cazenave, A. *et al.* The rate of sea-level rise. *Nature Climate Change* **4**, 358-361 (2014).
- 3 Hamlington, B. D. *et al.* Origin of interannual variability in global mean sea level. *Proceedings of the National Academy of Sciences* (2020).
- 4 Reager, J. *et al.* A decade of sea level rise slowed by climate-driven hydrology. *Science* **351**, 699-703 (2016).

- 5 He, X., Pan, M., Wei, Z., Wood, E. F. & Sheffield, J. A Global Drought and Flood Catalogue from 1950 to
2016. *Bulletin of the American Meteorological Society* **101**, E508-E535, doi:10.1175/bams-d-18-0269.1
(2020).
- 6 Lehner, B., Döll, P., Alcamo, J., Henrichs, T. & Kaspar, F. Estimating the impact of global change on flood
and drought risks in Europe: a continental, integrated analysis. *Climatic Change* **75**, 273-299 (2006).
- 7 Spinoni, J., Vogt, J. V., Naumann, G., Barbosa, P. & Dosio, A. Will drought events become more frequent
and severe in Europe? *International Journal of Climatology* **38**, 1718-1736,
doi:<https://doi.org/10.1002/joc.5291> (2018).
- 8 Ahmed, M., Sultan, M., Wahr, J. & Yan, E. The use of GRACE data to monitor natural and anthropogenic
induced variations in water availability across Africa. *Earth-Science Reviews* **136**, 289-300 (2014).
- 9 Phillips, T., Nerem, R., Fox-Kemper, B., Famiglietti, J. & Rajagopalan, B. The influence of ENSO on
global terrestrial water storage using GRACE. *Geophysical Research Letters* **39** (2012).
- 10 Pokhrel, Y. N. *et al.* Model estimates of sea-level change due to anthropogenic impacts on terrestrial water
storage. *Nature Geoscience* **5**, 389-392 (2012).
- 11 Rodell, M. *et al.* Emerging trends in global freshwater availability. *Nature* **557**, 651-659 (2018).
- 12 Yi, S., Sun, W., Feng, W. & Chen, J. Anthropogenic and climate-driven water depletion in Asia.
Geophysical Research Letters **43**, 9061-9069 (2016).
- 13 Boening, C., Willis, J. K., Landerer, F. W., Nerem, R. S. & Fasullo, J. The 2011 La Niña: So strong, the
oceans fell. *Geophysical Research Letters* **39** (2012).
- 14 Chen, J. L., Wilson, C. R. & Tapley, B. D. The 2009 exceptional Amazon flood and interannual terrestrial
water storage change observed by GRACE. *Water Resources Research* **46** (2010).
- 15 De Linage, C., Famiglietti, J. & Randerson, J. Statistical prediction of terrestrial water storage changes in
the Amazon Basin using tropical Pacific and North Atlantic sea surface temperature anomalies. *Hydrology
and Earth System Sciences* **18**, 2089-2102 (2014).
- 16 Fasullo, J. T., Boening, C., Landerer, F. W. & Nerem, R. S. Australia's unique influence on global sea level
in 2010–2011. *Geophysical Research Letters* **40**, 4368-4373 (2013).
- 17 Forootan, E. *et al.* Separation of large scale water storage patterns over Iran using GRACE, altimetry and
hydrological data. *Remote Sensing of Environment* **140**, 580-595 (2014).
- 18 Ni, S. *et al.* Global terrestrial water storage changes and connections to ENSO events. *Surveys in
Geophysics* **39**, 1-22 (2018).
- 19 Wolter, K. & Timlin, M. S. Measuring the strength of ENSO events: How does 1997/98 rank? *Weather* **53**,
315-324 (1998).
- 20 Chao, B. & Chung, C. On Estimating the Cross Correlation and Least Squares Fit of One Data Set to
Another With Time Shift. *Earth and Space Science* **6**, 1409-1415 (2019).
- 21 Hamlington, B. D. *et al.* The dominant global modes of recent internal sea level variability. *Journal of
Geophysical Research: Oceans* **124**, 2750-2768 (2019).
- 22 Kim, K.-Y., Hamlington, B. & Na, H. Theoretical foundation of cyclostationary EOF analysis for
geophysical and climatic variables: concepts and examples. *Earth-science reviews* **150**, 201-218 (2015).
- 23 Kim, K.-Y., North, G. R. & Huang, J. EOFs of one-dimensional cyclostationary time series: Computations,
examples, and stochastic modeling. *Journal of the atmospheric sciences* **53**, 1007-1017 (1996).
- 24 Mantua, N. J. & Hare, S. R. The Pacific decadal oscillation. *Journal of oceanography* **58**, 35-44 (2002).
- 25 Zhang, Y., Wallace, J. M. & Battisti, D. S. ENSO-like interdecadal variability: 1900–93. *Journal of climate*
10, 1004-1020 (1997).
- 26 Cheon, S.-H., Hamlington, B. D. & Suh, K.-D. Reconstruction of sea level around the Korean Peninsula
using cyclostationary empirical orthogonal functions. *Ocean Science* **14** (2018).
- 27 Gaughan, A. E., Staub, C. G., Hoell, A., Weaver, A. & Waylen, P. R. Inter-and Intra-annual precipitation
variability and associated relationships to ENSO and the IOD in southern Africa. *International Journal of
Climatology* **36**, 1643-1656 (2016).
- 28 Hamlington, B. *et al.* An ongoing shift in Pacific Ocean sea level. *Journal of Geophysical Research:
Oceans* **121**, 5084-5097 (2016).
- 29 Tang, Q. *et al.* Dynamics of terrestrial water storage change from satellite and surface observations and
modeling. *Journal of Hydrometeorology* **11**, 156-170 (2010).
- 30 Tapley, B. D., Bettadpur, S., Watkins, M. & Reigber, C. The gravity recovery and climate experiment:
Mission overview and early results. *Geophysical Research Letters* **31** (2004).

- 31 Watkins, M. M., Wiese, D. N., Yuan, D. N., Boening, C. & Landerer, F. W. Improved methods for
observing Earth's time variable mass distribution with GRACE using spherical cap mascons. *Journal of*
Geophysical Research: Solid Earth **120**, 2648-2671 (2015).
- 32 McCabe, M. F. *et al.* The future of Earth observation in hydrology. *Hydrology and Earth System Sciences*
21, 3879 (2017).
- 33 Landerer, F. W. *et al.* Extending the global mass change data record: GRACE Follow-On instrument and
science data performance. *Geophysical Research Letters* **47**, e2020GL088306 (2020).
- 34 Wiese, D. N., Landerer, F. W. & Watkins, M. M. Quantifying and reducing leakage errors in the JPL
RL05M GRACE mascon solution. *Water Resources Research* **52**, 7490-7502 (2016).
- 35 Wiese, D., Yuan, D., Boening, C., Landerer, F. & Watkins, M. JPL GRACE mascon ocean, ice, and
hydrology equivalent water height release 06 coastal resolution improvement (CRI) filtered version 1.0.
DAAC: Pasadena, CA, USA (2018).
- 36 Zhang, X. & Church, J. A. Sea level trends, interannual and decadal variability in the Pacific Ocean.
Geophysical Research Letters **39** (2012).
- 37 Hamlington, B. *et al.* The effect of the El Niño-Southern Oscillation on US regional and coastal sea level.
Journal of Geophysical Research: Oceans **120**, 3970-3986 (2015).
- 38 Yeo, S.-R. & Kim, K.-Y. Global warming, low-frequency variability, and biennial oscillation: an attempt to
understand the physical mechanisms driving major ENSO events. *Climate dynamics* **43**, 771-786 (2014).
- 39 Eicker, A., Forootan, E., Springer, A., Longuevergne, L. & Kusche, J. Does GRACE see the terrestrial
water cycle “intensifying”? *Journal of Geophysical Research: Atmospheres* **121**, 733-745 (2016).
- 40 Mandate, C. W. & Compact, U. G. Interactive Database of the World's River Basins [WWW Document].
URL [http://riverbasins.
wateractionhub.org/](http://riverbasins.wateractionhub.org/)(accessed 7.1. 19) (2016).
- 41 Hendy, E., Gagan, M. & Lough, J. Chronological control of coral records using luminescent lines and
evidence for non-stationary ENSO teleconnections in northeast Australia. *The Holocene* **13**, 187-199
(2003).
- 42 Lough, J. M. Tropical river flow and rainfall reconstructions from coral luminescence: Great Barrier Reef,
Australia. *Paleoceanography* **22** (2007).
- 43 Chowdhury, M. R. & Ward, N. Hydro-meteorological variability in the greater Ganges–Brahmaputra–
Meghna basins. *International Journal of Climatology: A Journal of the Royal Meteorological Society* **24**,
1495-1508 (2004).
- 44 Pervez, M. S. & Henebry, G. M. Spatial and seasonal responses of precipitation in the Ganges and
Brahmaputra river basins to ENSO and Indian Ocean dipole modes: implications for flooding and drought.
Natural Hazards and Earth System Sciences **15**, 147 (2015).
- 45 Chen, J. & Kumar, P. Role of terrestrial hydrologic memory in modulating ENSO impacts in North
America. *Journal of Climate* **15**, 3569-3585 (2002).
- 46 Entin, J. K. *et al.* Temporal and spatial scales of observed soil moisture variations in the extratropics.
Journal of Geophysical Research: Atmospheres **105**, 11865-11877 (2000).
- 47 Liang, Y. C., Lo, M. H. & Yu, J. Y. Asymmetric responses of land hydroclimatology to two types of El
Niño in the Mississippi River Basin. *Geophysical Research Letters* **41**, 582-588 (2014).
- 48 Lo, M. H. & Famiglietti, J. S. Effect of water table dynamics on land surface hydrologic memory. *Journal*
of Geophysical Research: Atmospheres **115** (2010).
- 49 Munoz, S. E. & Dee, S. G. El Niño increases the risk of lower Mississippi River flooding. *Scientific reports*
7 (2017).
- 50 Twine, T. E., Kucharik, C. J. & Foley, J. A. Effects of El Niño–Southern Oscillation on the climate, water
balance, and streamflow of the Mississippi River basin. *Journal of Climate* **18**, 4840-4861 (2005).

Figure legends

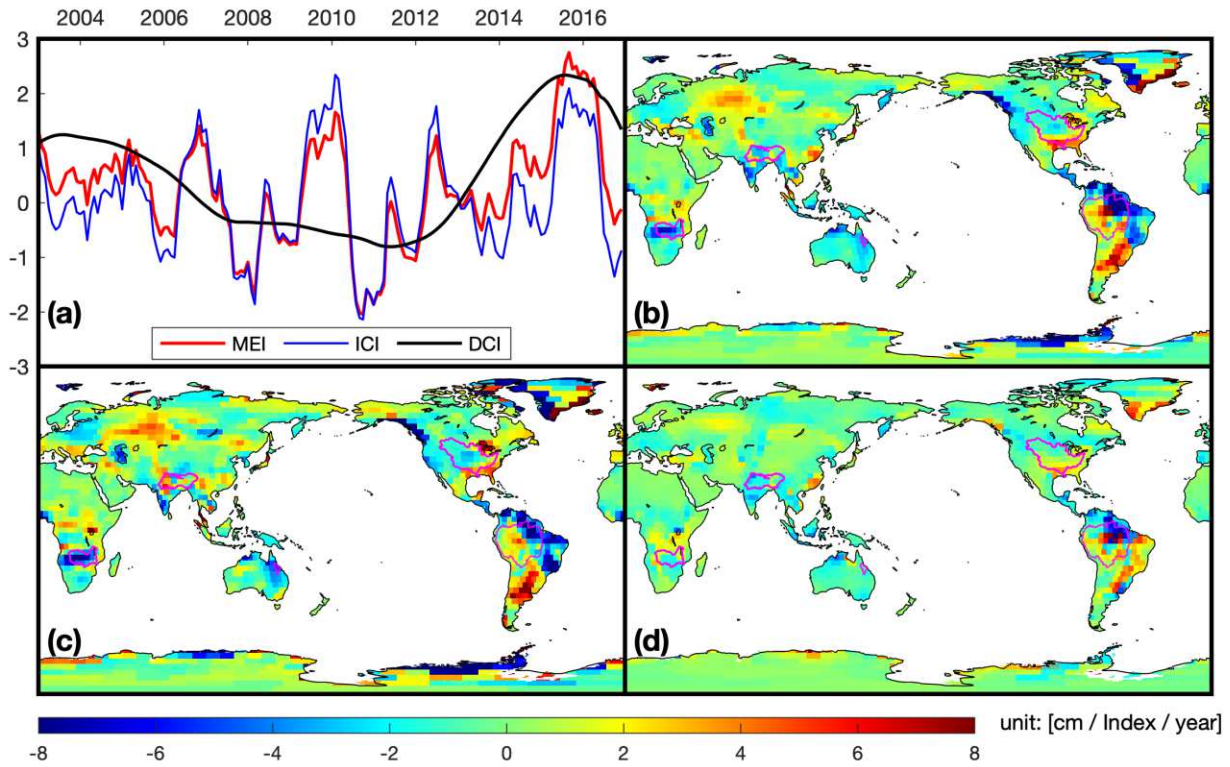


Figure 1. (a) ENSO Indices (MEI, DCI, and ICI; normalized by each standard deviation); the spatial map of influence of (b) MEI, (c) DCI, and (d) ICI from the LSR analysis (b: original LSR; c and d: modified LSR); the magenta-colored lines on the maps are five river-basins (see section 3.3).

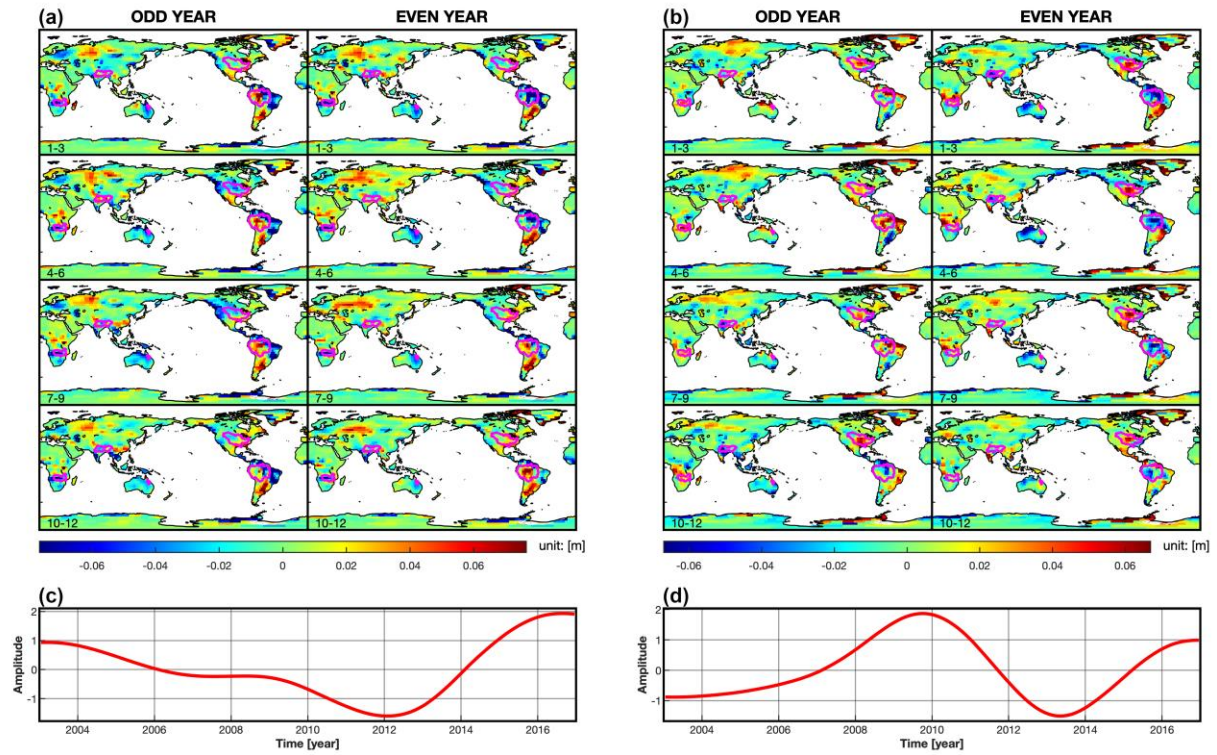


Figure 2. The dominant modes of the CSEOF analysis of GRACE: (a) LV of low-frequency mode (3 months averaged), (b) LV of high-frequency mode (3 months averaged), (c) PCT of low-frequency mode, and (d) PCT of high-frequency mode; the magenta-colored lines on the maps are five river-basins (see section 3.3); see Figure S2 and S3 for original LVs

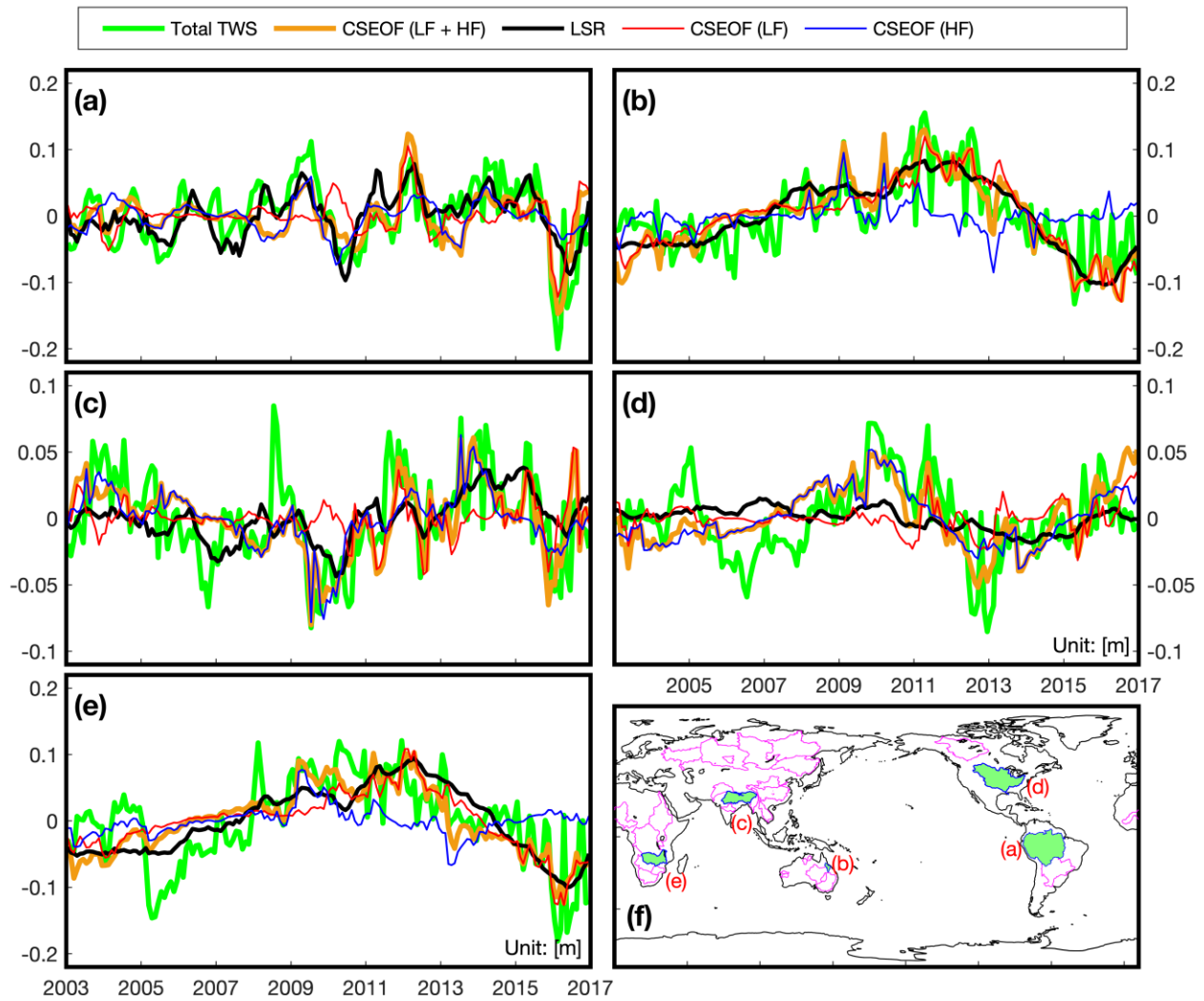


Figure 3. Spatial-mean time-series of regional ENSO-related TWS; (a) the Amazon River, (b) the Burdekin River, (c) the Ganges Brahmaputra River, (d) the Mississippi River, (e) the Zambezi River, and (f) the location of each river-basin (green-filled areas: a ~ e and magenta lines: for Table 1); Green: total TWS, Orange: ENSO-related TWS by CSEOF (LF + HF), Black: ENSO-related TWS by LSR, Red: CSEOF LF-mode, Blue: CSEOF HF-mode.

Tables

Table 1. Percentage of the variance of total TWS explained for river-basins around the world.

Basins	LSR				CSEOF		
	PH12	Current Study			HF	LF	HF + LF
	MEI	ICI	DCI	DCI+ICI			
(a) Amazon	<u>44.3</u>	<u>34.4</u>	<u>11.2</u>	<u>45.6</u>	<u>20.4</u>	<u>28.7</u>	<u>49.1</u>
Amur	<u>5.3</u>	<u>2.4</u>	<u>11.8</u>	<u>14.2</u>	<u>11.7</u>	<u>14.0</u>	<u>25.7</u>
(b) Burdekin	<u>32.9</u>	<u>7.5</u>	<u>57.8</u>	<u>65.3</u>	<u>10.6</u>	<u>62.9</u>	<u>73.5</u>

Congo	<u>7.7</u>	<u>8.5</u>	<u>1.3</u>	<u>9.8</u>	<u>32.1</u>	<u>9.8</u>	<u>41.9</u>
Eyre lake	<u>17.5</u>	<u>5.8</u>	<u>30.5</u>	<u>36.3</u>	<u>4.9</u>	<u>41.9</u>	<u>56.8</u>
(c) GangesBrahmaputra	<u>10.4</u>	<u>10.4</u>	<u>12.2</u>	<u>22.6</u>	<u>37.1</u>	<u>14.8</u>	<u>51.9</u>
Gascoyne	<u>30.9</u>	<u>24.9</u>	<u>11.1</u>	<u>36.0</u>	<u>38.4</u>	<u>15.7</u>	<u>54.1</u>
Godavari	<u>10.9</u>	<u>18.8</u>	<u>2.6</u>	<u>21.4</u>	<u>23.7</u>	<u>10.1</u>	<u>33.8</u>
Hwang he	<u>5.4</u>	<u>1.8</u>	<u>8.8</u>	<u>10.6</u>	<u>13.4</u>	<u>12.1</u>	<u>25.4</u>
Indus	<u>8.6</u>	<u>2.7</u>	<u>18.2</u>	<u>20.9</u>	<u>8.6</u>	<u>27.8</u>	<u>36.4</u>
Irrawaddy	<u>9.8</u>	<u>7.7</u>	<u>3.8</u>	<u>11.5</u>	<u>11</u>	<u>15.6</u>	<u>26.6</u>
Lena	<u>5.8</u>	<u>3.9</u>	<u>8.7</u>	<u>12.6</u>	<u>9.4</u>	<u>8.6</u>	<u>18</u>
Limpopo	<u>15.9</u>	<u>13.5</u>	<u>4.9</u>	<u>18.5</u>	<u>12.9</u>	<u>11.9</u>	<u>24.8</u>
Mackenzie	<u>21.2</u>	<u>14.8</u>	<u>15.1</u>	<u>29.8</u>	<u>10.0</u>	<u>23.3</u>	<u>33.3</u>
Mekong	<u>15.2</u>	<u>15.4</u>	<u>2.5</u>	<u>17.9</u>	<u>16.3</u>	<u>26.8</u>	<u>43.1</u>
(d) Mississippi	<u>3.2</u>	<u>2</u>	<u>5.1</u>	<u>7.1</u>	<u>40.5</u>	<u>11</u>	<u>51.5</u>
Murchison	<u>37.5</u>	<u>23.9</u>	<u>22.3</u>	<u>46.3</u>	<u>31.3</u>	<u>26.8</u>	<u>58.1</u>
Murray-Darling	<u>19.4</u>	<u>9.9</u>	<u>20.7</u>	<u>30.6</u>	<u>17.7</u>	<u>29.2</u>	<u>46.9</u>
Niger	<u>28.4</u>	<u>17.2</u>	<u>19.8</u>	<u>37</u>	<u>19.8</u>	<u>34</u>	<u>53.8</u>
Nile	<u>3.4</u>	<u>3.3</u>	<u>18.8</u>	<u>22.1</u>	<u>12.1</u>	<u>31.5</u>	<u>43.6</u>
OB	<u>30.1</u>	<u>7.4</u>	<u>54.3</u>	<u>61.8</u>	<u>9.9</u>	<u>60.1</u>	<u>70.1</u>
Okavango	<u>31.5</u>	<u>13.2</u>	<u>45.9</u>	<u>59.1</u>	<u>10.5</u>	<u>50.9</u>	<u>61.4</u>
Orange	<u>19.1</u>	<u>8.8</u>	<u>32.7</u>	<u>41.5</u>	<u>5</u>	<u>42.6</u>	<u>47.6</u>
Parana	<u>28.9</u>	<u>14.6</u>	<u>25.7</u>	<u>40.4</u>	<u>24.0</u>	<u>23.5</u>	<u>47.5</u>
Roper	<u>13.4</u>	<u>11.7</u>	<u>6.2</u>	<u>18.0</u>	<u>29.6</u>	<u>15.8</u>	<u>45.4</u>
Victoria	<u>17</u>	<u>15.3</u>	<u>6.7</u>	<u>22.0</u>	<u>34.6</u>	<u>17.1</u>	<u>51.7</u>
Volga	<u>13.8</u>	<u>6</u>	<u>16.4</u>	<u>22.4</u>	<u>5.7</u>	<u>29.4</u>	<u>35.2</u>
Yangtze	<u>14.3</u>	<u>12</u>	<u>7.9</u>	<u>19.9</u>	<u>10.7</u>	<u>16.6</u>	<u>27.2</u>
Yenisei	<u>2.2</u>	<u>2.2</u>	<u>0.9</u>	<u>3.0</u>	<u>21.1</u>	<u>13.5</u>	<u>34.6</u>
(e) Zambezi	<u>24.9</u>	<u>4.8</u>	<u>51.7</u>	<u>56.5</u>	<u>10.0</u>	<u>45.6</u>	<u>55.6</u>

Competing interests

The authors declare no competing interests.

Acknowledgements

The research was carried out at the Jet Propulsion Laboratory, California Institute of Technology, under a contract with the National Aeronautics and Space Administration.

Author contributions

S.C. and B.H. conceived the study together; S.C. conducted the analysis and wrote the manuscript; B.H. supervised this study; J.R. and H.C. reviewed the manuscript.

Figures

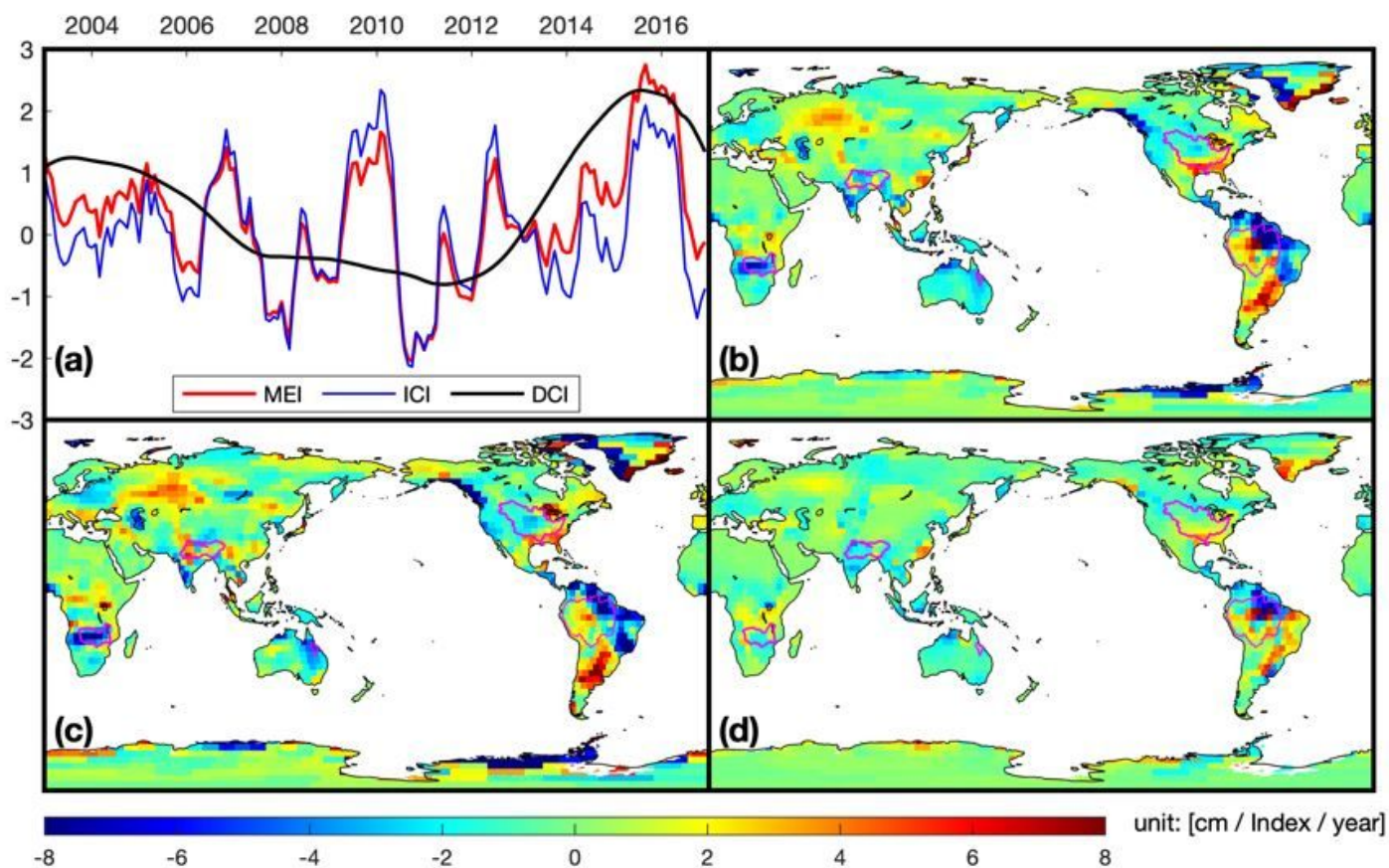


Figure 1

(a) ENSO Indices (MEI, DCI, and ICI; normalized by each standard deviation); the spatial map of influence of (b) MEI, (c) DCI, and (d) ICI from the LSR analysis (b: original LSR; c and d: modified LSR); the magenta-colored lines on the maps are five river-basins (see section 3.3). Note: The designations employed and the presentation of the material on this map do not imply the expression of any opinion whatsoever on the part of Research Square concerning the legal status of any country, territory, city or area or of its authorities, or concerning the delimitation of its frontiers or boundaries. This map has been provided by the authors.

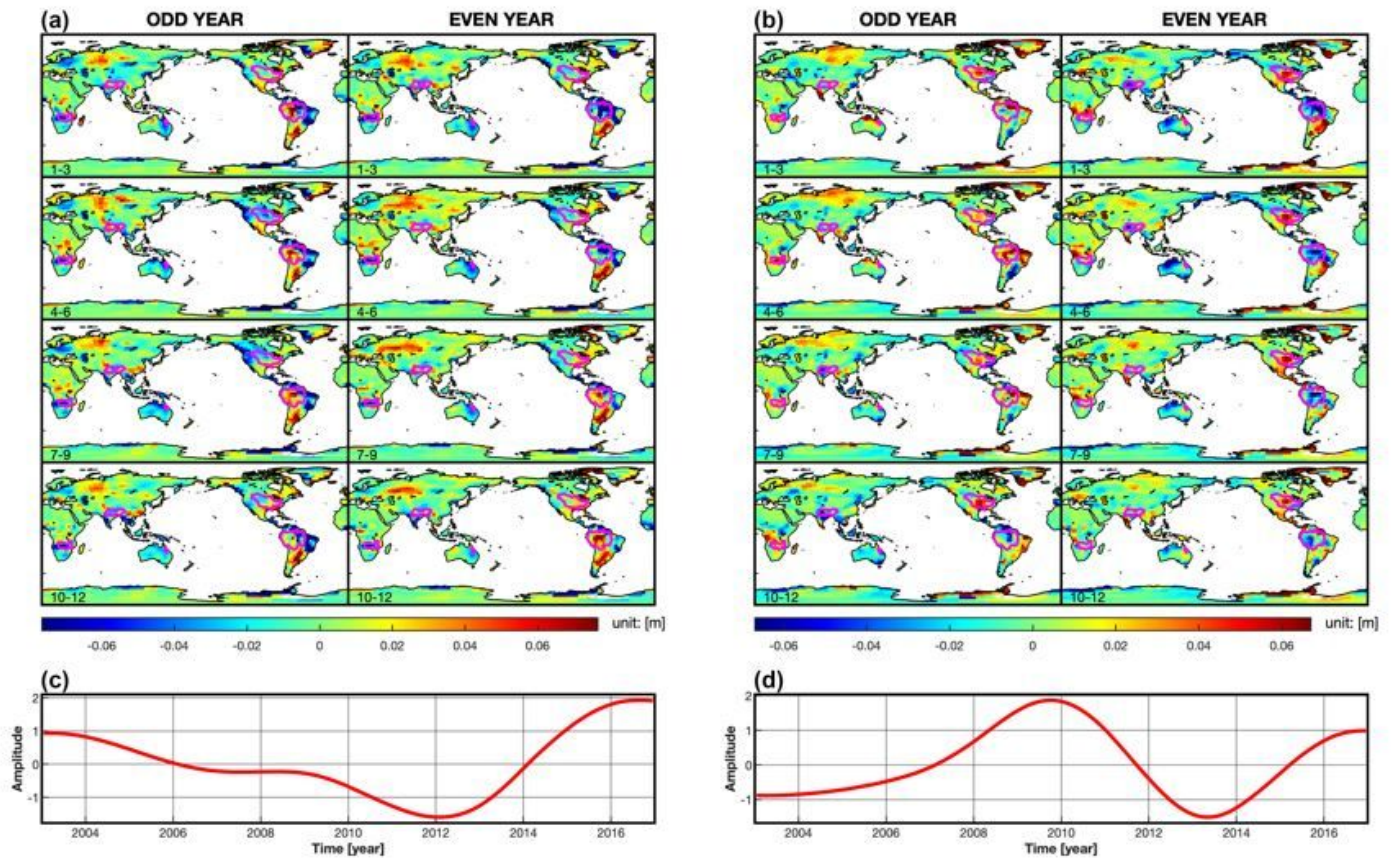


Figure 2

The dominant modes of the CSEOF analysis of GRACE: (a) LV of low-frequency mode (3 months averaged), (b) LV of high-frequency mode (3 months averaged), (c) PCT of low-frequency mode, and (d) PCT of high-frequency mode; the magenta-colored lines on the maps are five river-basins (see section 3.3); see Figure S2 and S3 for original LVs Note: The designations employed and the presentation of the material on this map do not imply the expression of any opinion whatsoever on the part of Research Square concerning the legal status of any country, territory, city or area or of its authorities, or concerning the delimitation of its frontiers or boundaries. This map has been provided by the authors.

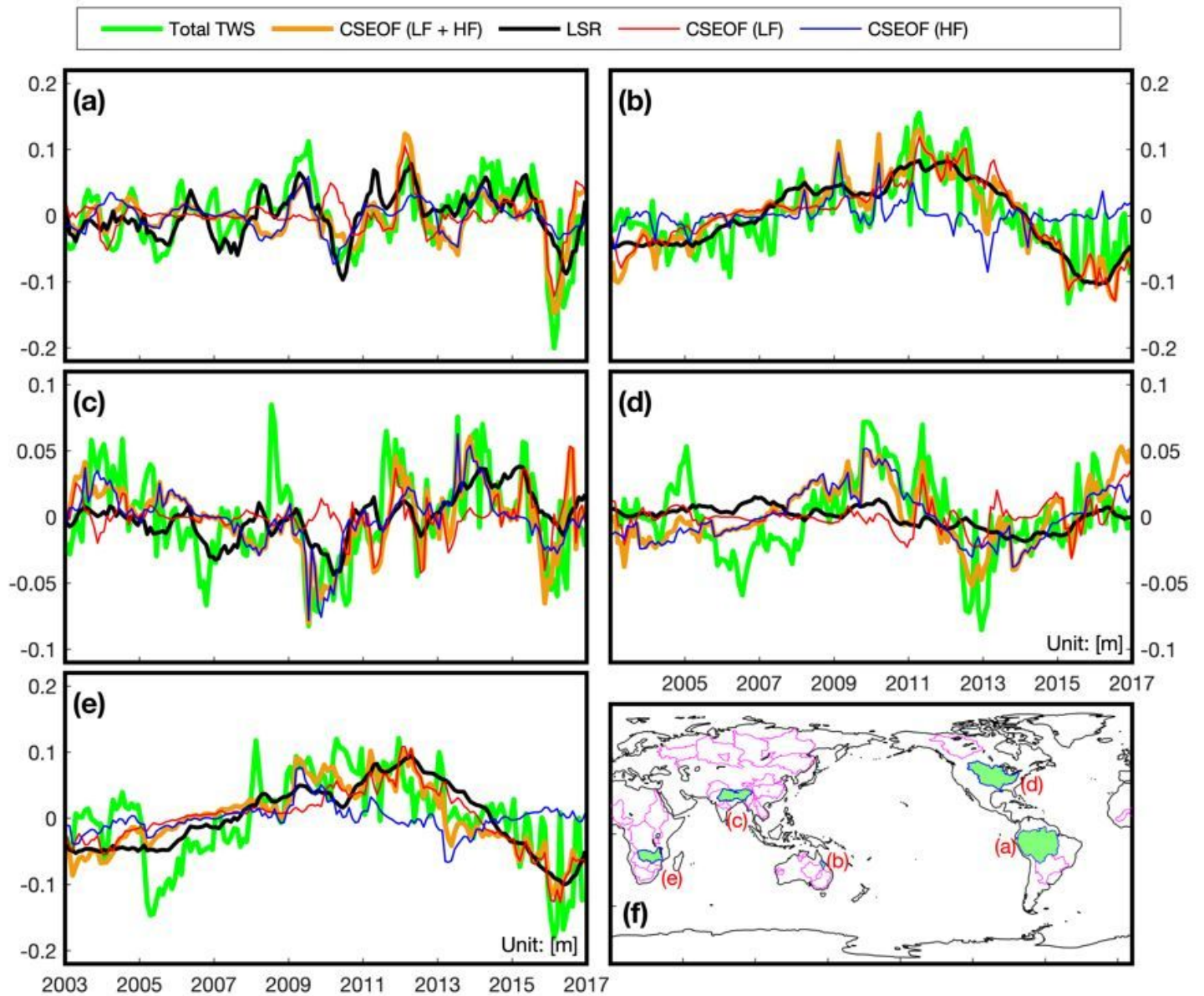


Figure 3

Spatial-mean time-series of regional ENSO-related TWS; (a) the Amazon River, (b) the Burdekin River, (c) the Ganges Brahmaputra River, (d) the Mississippi River, (e) the Zambezi River, and (f) the location of each river-basin (green-filled areas: a ~ e and magenta lines: for Table 1); Green: total TWS, Orange: ENSO-related TWS by CSEOF (LF + HF), Black: ENSO-related TWS by LSR, Red: CSEOF LF-mode, Blue: CSEOF HF-mode. Note: The designations employed and the presentation of the material on this map do not imply the expression of any opinion whatsoever on the part of Research Square concerning the legal status of any country, territory, city or area or of its authorities, or concerning the delimitation of its frontiers or boundaries. This map has been provided by the authors.

Supplementary Files

This is a list of supplementary files associated with this preprint. Click to download.

- [TWSENSOSupplementSciRepv100.docx](#)